

Cosmic ray simulator: A versatile apparatus for quantitative studies on the interaction of cosmic rays with frozen solids by on line and *in situ* quadrupole mass spectrometry and Fourier transform infrared spectroscopy

R. I. Kaiser,^{a)} A. Gabrysch, and K. Roessler
Institut für Nuklearchemie, Forschungszentrum Jülich, 52425 Jülich, Germany

(Received 22 June 1994; accepted for publication 4 January 1995)

The cosmic ray simulator consists of a 50 cm cylindrical stainless steel chamber. A rotatable cold finger milled of a silver (111) monocrystal optimizes heat conductivity and is connected to a programmable, closed cycle helium refrigerator allowing temperature control of an attached silver wafer between 10 and 340 K (± 0.5 K). Oil-free ultrahigh vacuum (UHV) conditions of $\approx 10^{-10}$ mbar are provided by a membrane, drag, and cryopump, hence guaranteeing a vacuum system free of any contamination. Ice layers of defined crystal structures and reproducible thickness of (5 ± 1) μm are achieved by depositing gases, e.g., CH_4 , CD_4 , CD_4/O_2 , and CH_4/O_2 , with a computer-assisted thermostated valve on the cooled wafer. These frosts are irradiated at 10 and 50 K with 7.3 MeV protons and 9 MeV α particles of the compact cyclotron CV28 in Forschungszentrum Jülich up to doses of 150 eV per molecule, i.e., simulating the distribution maximum of galactic cosmic ray particles interacting with primordial matter in space during 0.7×10^9 yr. During the experiments, gas phase and solid state are monitored for the first time quantitatively on line and *in situ* by a quadrupole mass spectrometer (QMS) via matrix interval arithmetic and a Fourier transform infrared spectrometer (FTIR) in an absorption-reflection mode at 62.5° . For the first time, a cosmic ray simulator allows detailed and reproducible mechanistic studies on the interaction of cosmic ray particles with frozen gases in space based on pressure conditions (hydrocarbon free UHV conditions, the limitation of condensations of residual gases during an experiment to less than one monolayer), temperature regime (the use of silver monocrystals, FTIR in reflection, optimized ion currents, and target thicknesses < 5 μm restrict temperature increasing to 14 K), and defined target systems. In combination with two on line and *in situ* analyses techniques, i.e., FTIR and QMS, the machine yields unprecedented options such as computing the heating of the ice surfaces directly exposed to the ion beam by a calibrated QMS and a complete quantification of product distribution. Preliminary results indicate a strong temperature-dependent component of the reaction mechanisms in the frosts: surface layers are heated by impinging ions to (14 ± 1) K and yield (70%–100%) of higher molecular weight species, such as $\text{C}_{11}\text{D}_{24}$, whereas 10 K regions produce majority of simpler hydrocarbons, e.g., C_3D_8 . Second, O_2 contaminations influence the experiments dramatically by trapping of diffusive H atoms as O_2H and, thus, yield oxygen-containing yellow to brown residues after heating to 293 K. Irradiation of pure methane targets, however, produce no residues. But an increasing concentration of H atoms exceeding $(6\% \pm 3\%)$ leads to ejection of up to 90% of the frosts into vacuum. © 1995 American Institute of Physics.

I. INTRODUCTION

Space is interspersed with high energetic particles and photons of solar and galactic cosmic rays,¹ flares,² T Tauri winds,³ stellar jets,⁴ carbon stars,⁴ energetic species in magnetospheres of giant planets,⁵ and photodissociation products.⁵ These species modify primordial and still processed matter of planets, their moons and rings, asteroids, comets, and interstellar grains or clouds by suprathreshold chemistry⁶ and photochemistry. Additionally, catalysis on grain surfaces⁷ and perhaps aqueous chemistry in heated comets (Strecker synthesis of amino acids,⁸ CP-, CS-, and HCN-polymer hydrolysis)⁹ contribute to their complexation and, thus, modify the chemical and physical properties of primordial matter in space. Further, Fischer–Tropsch synthesis in

the accretion disc of the solar system¹⁰ and pyrite catalyzed reactions¹¹ have been postulated to advance the syntheses of organic molecules.

Enormous interest is given to detailed mechanisms forming complex molecules in space, the latter might be considered as precursors of biological active molecules such as adenine or guanine. In particular, the interaction of high energetic radiation with hydrocarbons in the solid state and mixtures of water, carbon monoxide, methane has been studied for three decades, all resulting in the formation of new molecules.^{12–22} Polycyclic aromatic hydrocarbons, among the most fascinating, are formed during methane irradiations with MeV α particles at 10 K.^{23–25}

These simulations of extraterrestrial environments occur in so-called *simulation chambers* and require analogous temperatures, pressures, and high energy components of the cosmic radiation field. Predominantly, chambers are evacuated by oil-containing roughing pumps and lubricated turbomo-

^{a)}Present address: Dept. of Chemistry, University of California, Berkeley, CA 94720.

lecular pumps to high vacua of 10^{-8} – 10^{-6} mbar. Liquid helium cryostats or closed cycle helium refrigerators cool mounted cold fingers down to 10 K. Typically, the latter consist of polycrystalline aluminum, copper, or stainless steel and serve as sample holders for Si, KBr, or CsJ windows to monitor the gas condensation and effects of subsequent irradiation by MeV or keV particles, UV photons, electron beams, ^{60}Co - γ -quants, or radio frequency discharges by Fourier transform infrared spectroscopy (FTIR). Optionally, gas phases are monitored by quadrupole mass spectrometers (QMS).

Nevertheless, current experimental conditions are often rather nebulous. First, the cooled substrates and the ices serve as cold traps for residual gases, e.g., H_2O , O_2 , N_2 , and CO_2 : pressures of about 10^{-7} mbar allow gas molecules to condense one monolayer within less than one minute. In spite of generating frosts by depositing gases at approximately 10^{-5} mbar, up to 1% of the contaminants are cocondensed. In particular, molecular oxygen limits the credibility of the experiments dramatically and changes the mechanism for the formation of complex molecules: during exposing methane frosts to, for example, MeV protons,²⁶ oxygen is fixed in molecules as shown by infrared stretching vibrations of carbonyl (1800 – 1700 cm^{-1}) and hydroxyl groups (3800 – 3000 cm^{-1}). Further, vacuum systems operated with oil sealed roughing pumps require fluid to operate and, consequently, are sources of contamination, i.e., the erroneous detection of “synthesized” polycyclic aromatic hydrocarbons.²⁷

Second, neither employed polycrystalline metal targets and IR transmission components nor condensed layers thicker than $\approx 10\ \mu\text{m}$ guarantee a constant temperature in the target: the latter two materials hold thermal conductivities of $\lambda=0.1$ – $0.01\text{ W cm}^{-1}\text{ K}^{-1}$,²⁸ and, thus, act as thermal insulators unable to prevent heating of the frosts by impinging ions from 10 up to 50 K.^{5,16,17} Consequently, heating increases both the temperature-dependent diffusion coefficient of generated radicals such as H, CH, CH_2 , CH_3 , OH, and induces sublimation of molecules, modifying the chemical composition of the target and the reaction mechanisms.

Therefore, existing experimental setups hardly allow detailed and reproducible mechanistic studies on the interaction of cosmic rays with frozen matter in space. The new apparatus to be constructed has to fulfill the following requirements, i.e., (a) oil free ultrahigh vacua (UHV) to guarantee a clean experimental setup without hydrocarbons and cocondensates, (b) reproducible preparation of thin frost layers, (c) optimal cooling of the frosts to minimize heating, i.e., thin ice layers and alternative components for FTIR analyses, (d) temperature monitoring of heated ice surfaces and substrates, and (e) quantitative on line and *in situ* analyses of the solid state and the gas phase.

This paper is organized as follows: Secs. II A–II C compile theoretical restrictions of the simulation chamber (pressures and temperatures), followed by a detailed description of the machine itself, analytical instruments, and the gas mixing chamber. Sections II D and II E depict the operating procedure and analyze experimental conditions. Finally, a

discussion with focused interest on elaborated requirements (a)–(d) is presented in Sec. III.

II. EXPERIMENTAL SETUP

A. Design principles

Residual gases condensing on the cooled wafer and heating of the irradiated sample influence the results of the experiments dramatically. The surface of each silver wafer used in the experiments contains approximately $(1\pm 0.5)10^{19}$ atoms m^{-2} . If we assume the gas phase consists only of molecules at $T=293\text{ K}$ with sticking coefficients α (molecule)=1 at 10 K, one monolayer condenses within $\approx 10\text{ h}$ at 10^{-10} mbar. This is an order of magnitude time for the interval each experiment has to be executed.

The temperature profile of the frosts, expressed as the temperature difference between the heated ice surface directly exposed to the ion beam, T_{ion} , and the backsurface in contact with the cold finger, T_{back} , is a crucial parameter in diffusion controlled processes and might influence the reaction mechanisms and the product distribution extremely. The MeV ion beam heats the surface from T_{before} to T_{ion} , and, consequently, raises the temperature-dependent vapor pressure of the condensed frosts. Hence, calibrating the vapor pressure by heating the frosts in 0.5 K steps from 9 to 20 K and recording ion currents $I(T)$ of the molecular fragments by a quadrupole mass spectrometer determines the surface temperature. During these external calibrations, the sample is allowed to equilibrate 30 min after each 0.5 K increment. Hence, a negligible temperature gradient exists between the ice surface exposed to the vacuum and the cold finger, whose T_{cold} is measured by an attached silicon diode. Fitting $I(T)$ with $I(T_{\text{ion}})$ yields the surface temperature of the frosts dur-

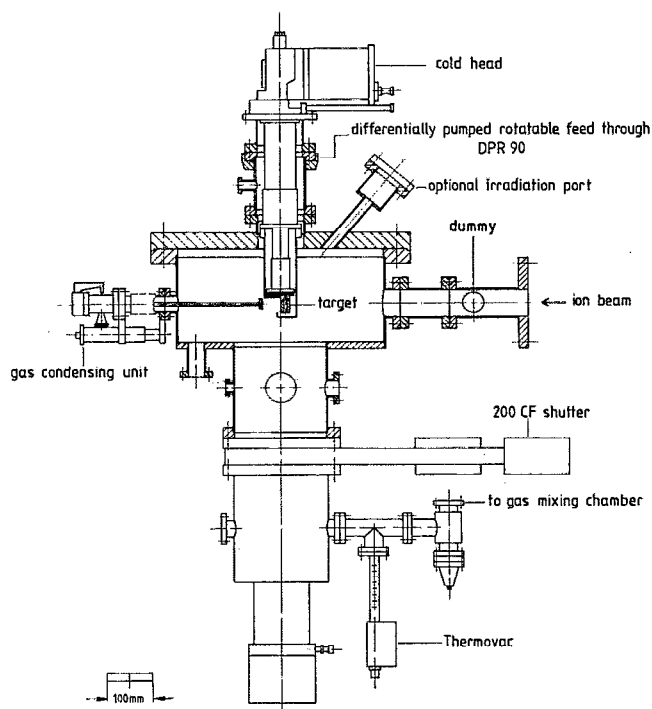


FIG. 1. Sideview of the simulation chamber.

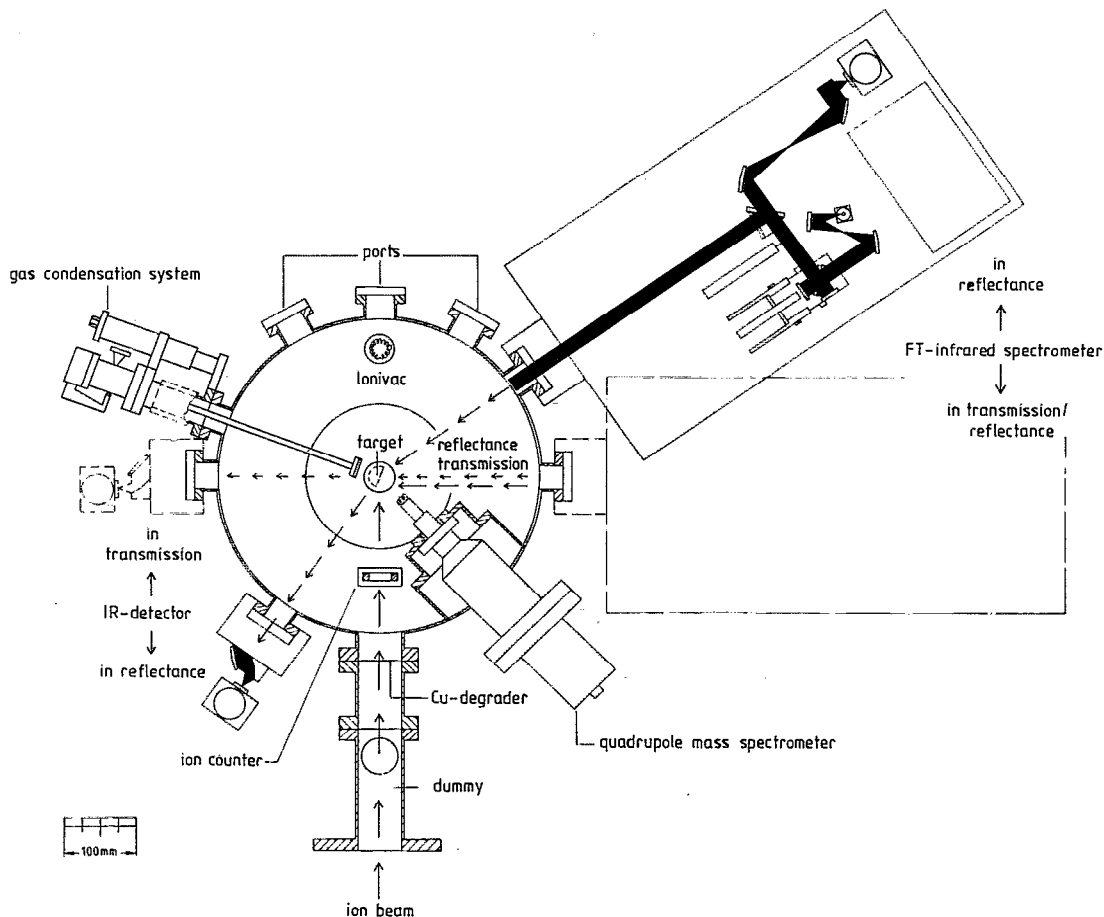


FIG. 2. Top view of the simulation chamber.

ing each irradiation and allows extraction of temperature effects. This procedure approximates a mole fraction of target molecules x and their activity coefficients f in freshly deposited as well as irradiated samples as x (target molecules) = f (target molecules) = 1. However, the fact that only 1% of deposited molecules are converted to products justifies this approach.

Additionally, using monocrystalline cold fingers accelerate heat transfer to the cooling system, and, consequently, reduce heating of the frosts. Silver (111) monocrystals, hereafter referred to as Ag-(111), represent an optimal compromise between heat conductivity from the cold finger to the closed cycle helium refrigerator, and material hardness.^{29,30} Therefore, FTIR analyses of condensed frosts must be executed in reflection mode because silver represents a non-IR-transmission component.

B. Simulation chamber

The simulation chamber consists of a cylindrical stainless steel cylinder of 40 cm diam and 21 cm height with nine centro symmetrical 35 CF ports and one 63 CF port (Figs. 1 and 2). A 400 CF flange shuts the lid of the vessel and holds a centered, differentially pumped rotatable feed through DPR 90 (VG-Instruments). This construction enables an attached CP1020 closed cycle helium refrigerator (Cryophysics) to

rotate horizontally 360°. The cold finger consists of an Ag-(111) monocrystal (99.999%, Degussa) and is fixed via a 0.1 mm indium foil to the 10 K step of the cold head. To minimize the radiative heat transfer from the room temperature chamber walls to the 10 K stage, a 30–40 K aluminum radiation shield connected with the cold head's second stage surrounds the crystal. The cold finger serves as a substrate for a (25×25) mm², 3 mm thick and high polished, i.e., corn size <1 μm, Ag-(111) wafer, the last fixed by screws via a 0.1-mm-thick indium foil to the cold finger. This setup assists a quick change of the wafer after each experiment without demounting the whole cold finger. The temperature of the monocrystal is sampled by a silicon diode DT-470-CO (resistance $R=10^5 \Omega$; current $I=10 \mu\text{A}$) (Lake Shore), thus, facilitating any choice between 10 and 350 K with the help of a 50 Ω heater and a programmable temperature controller 93-CA (Lake Shore).

All frosts are condensed on a circular area ($\varnothing=20$ mm) on the Ag-(111) wafer by a gas deposition system which is mounted onto a linear transfer mechanism (VG Instruments). Hereby, the gas molecules streaming out of the gas mixing chamber (see Sec. II C) pass the thermo valve UDV 235 T (Balzers), enter a stainless steel capillary and are deposited after leaving a glass capillary array (Spectroscopy Instruments). Both the limited pore size of 10 μm and the ratio of

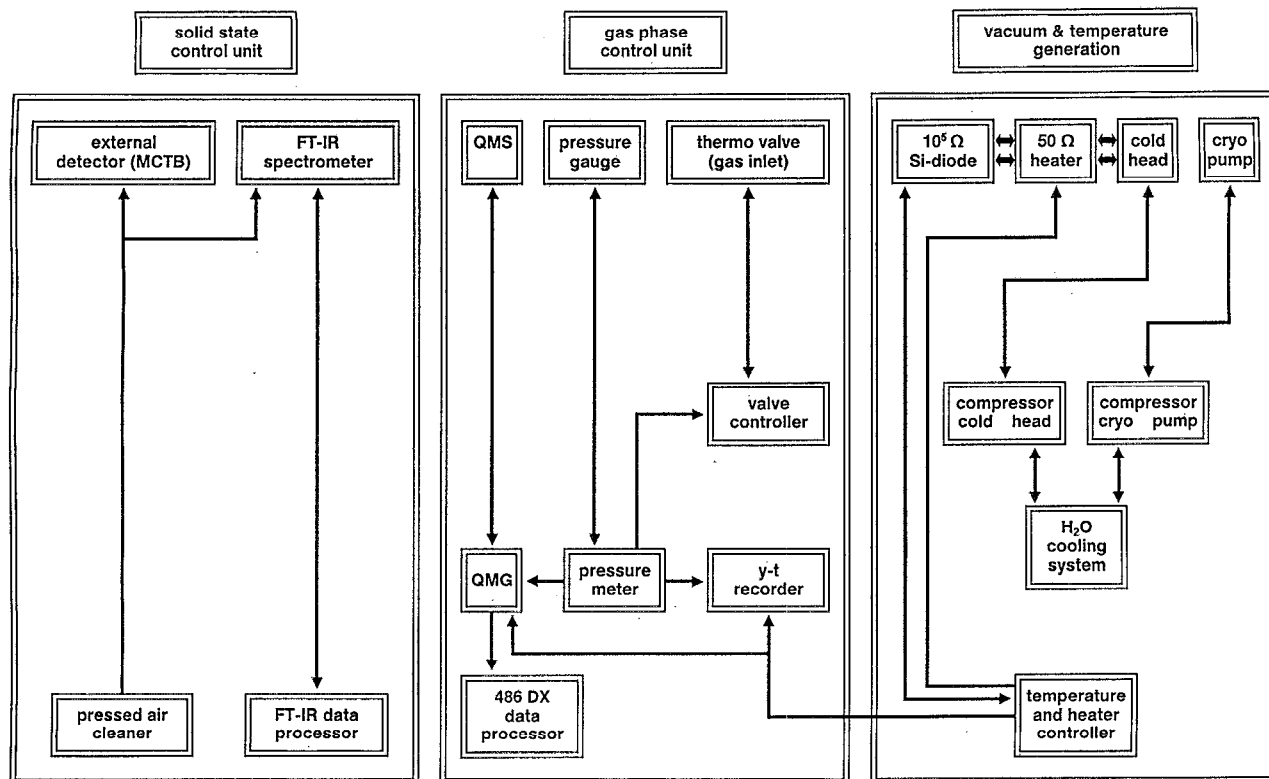


FIG. 3. Control diagram of the simulation chamber and periphery instruments.

the array area to the sum of pore size of 0.5 guarantee a homogeneous gas deposition.

The dummy unit constitutes the interface between the chamber and the beam line of the cyclotron: it consists of a Faraday cup and an integrated oxygen-free high-conductivity copper degrader (thickness $d=0.1$ mm) and separates the UHV system of the recipient from the oil containing high vacuum of the cyclotron. All ion beams are adjusted by an electrically isolated Faraday cup serving as a full beam stop and conducting the striking ions to the current integrator of the cyclotron control unit, i.e., monitoring the beam current. The heat generated in the course of the adjustment is drawn off by a closed cycle cooling water, distilled to minimize blind currents. Before the irradiation, the Faraday cup has to be lowered; the ion current and beam profile are controlled via a nickel grid mounted between the copper degrader and the target, connected with a second current integrator. To eliminate currents from the grid to the chamber, the nickel wire is insulated by a MACOR ceramic (ratio of the grid surface to the surface varnished by the beam: 0.015).

Further on, a cryopump KM 212 (pump speed $S=1500 \text{ } \ell s^{-1}$, Balzers) is mounted at the bottom of the recipient and is separable from the main chamber by a 200 CF shutter. This pump is connected via two valves with the gas mixing chamber and an oil-free roughing pump system consisting of a membrane pump, molecular drag pump, and turbomolecular pump (DRYTEL 25, $S=7.5 \text{ } \ell s^{-1}$, ultimate vacuum $\sim 10^{-5}$ mbar, ALCATEL). The last one evacuates the DPR 90 differentially, too, and reduces the pressure gradient from 1013 mbar (surrounding atmosphere) over 10^{-5} mbar (roughing pump) to 10^{-10} mbar. Pressures between 10^3

and 10^{-3} mbar are monitored by THERMOVACs, those in the range of 10^{-5} – 10^{-12} mbar by IONIVACs (extractor mode). The remaining 35 CF blank flanges can be used in future experiments for extra analytical instruments, e.g., modular irradiation sources such as laser beams, keV ion guns, and UV photons.

The complete apparatus is wrapped with heating tapes and aluminum foil for baking the chamber. Integrated feedback systems monitor the temperature in each chamber section, i.e., $75 \text{ } ^\circ\text{C}$ (cold head and DPR 90), $70 \text{ } ^\circ\text{C}$ (400 CF flange), $65 \text{ } ^\circ\text{C}$ (linear transfer mechanism and middle part of the chamber), $60 \text{ } ^\circ\text{C}$ (bottom and 200 CF shutter) $55 \text{ } ^\circ\text{C}$ (cryopump). Finally, the gas mixing chamber is baked at $100 \text{ } ^\circ\text{C}$. Figure 3 summarizes the simulation chamber and its periphery instruments.

Ion beam induced chemical modifications are analyzed on line and *in situ* by a FTIR spectrometer (NICOLET 510 DX) in the spectral region of $4000\text{--}400 \text{ cm}^{-1}$: the IR beam ($\varnothing=30$ mm) is deflected by a software controlled mirror flipper out of the spectrometer, passes an aperture of eloxized aluminum ($\varnothing=25$ mm), and enters the simulation chamber through a KBr window attached to an UHV compatible 35 CF flange. After diffuse reflection of the IR beam at the vacuum-frost boundary and being absorbed by the ices, the beam is reflected at the polished Ag-(111) wafer [reflection angle= $(62.5^\circ \pm 0.1^\circ)$, cf. Fig. 4]. The IR beam is attenuated by the condensates again, passes a second KBr window placed 35° counterclockwise to the dummy unit, and is analyzed by an external, liquid nitrogen cooled mercury-cadmium-telluride (Nicolet Instruments, detector type B) (MCTB) detector. To reduce IR absorption by atmo-

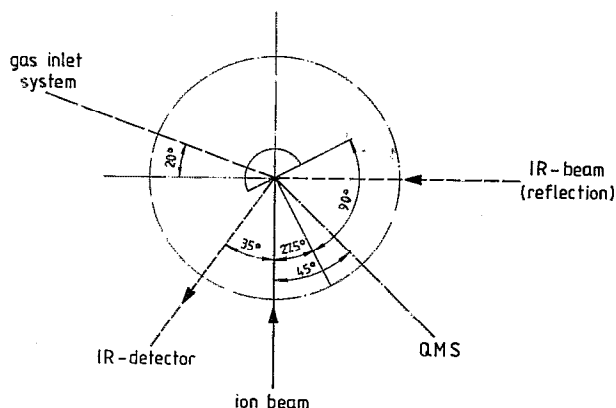


FIG. 4. Geometry of the FTIR-absorption-reflection measurements.

spheric gases, e.g., CO_2 and H_2O , the spectrometer and the detector are flushed by oil, water, and carbon dioxide free compressed air.

Volatile species are detected by a quadrupole mass spectrometer type QMG 420 (Balzers) situated 45° counterclockwise in respect to the dummy unit [angle between Ag-(111) wafer perpendicular-field axes of QMS $\varphi=17.5^\circ$]. Analog and digital voltages are generated by the electronic unit QME 112 (mass range 1–200 amu), whereas the analyzer consists of a molybdenum quadrupole rod system QMA 120 biased at 5.25 V with an axial beam source, rhenium cathode (60 V, emission current 0.8 mA), and a secondary electron multiplier (SEM, 1400 V), whereas the cathode potential was held at 150 V, thus, generating 90 eV electrons. Finally, scan velocities were optimized to $0.5\text{--}1\text{ s amu}^{-1}$ and electronic background subtraction was chosen at $m/z=5.5$.

C. Gas mixing chamber

Gas mixtures must be prepared in so-called mixing chambers, i.e., setups for heating binary or higher ordered mixtures under continuous stirring and ensuing cooling. In the course of their preparation, convective flows are induced homogenizing the gases appreciably faster than diffusion controlled processes at room temperature. Typically, a 2 ℓ UHV gas mixing chamber is welded from two 100 CF flanges and a stainless steel spacer. An UHV compatible motor driven feed through moving a rotor inside the chamber is attached at the lid of the mixing chamber. Four UHV valves (three adapters for gas containers, one tube to the gas deposition system) and a 35 CF shutter connect this chamber with the recipient and the pump system. Partial pressures of the gases are measured by a gas type independent capacitive pressure gauge MI 2000 (Leybold).

D. Operating procedure

The roughing pump system and the cryopump evacuate the simulation chamber and the gas mixing chamber to about 10^{-8} mbar. Subsequently, the gas mixing chamber is filled with gas(es); in the case of mixtures, the mixing chamber is heated for 2 h at 100°C and cooled down within additional 60 min. The thermo valve connecting the gas mixing chamber and the recipient is opened until the pressure indicates

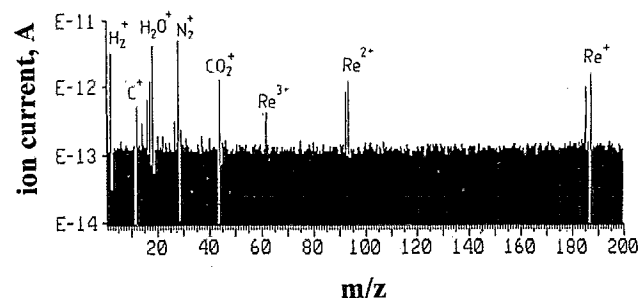


FIG. 5. Typical mass spectrum of residual gases at a pressure of 3.5×10^{-10} mbar.

5×10^{-6} mbar. After adjusting the heating current of the thermo valve until the pressure levels to about 10^{-8} mbar, the pressure required for the gas condensation is optimized to 10^{-6} mbar.

Afterwards, the DPR rotates the Ag-(111) wafer parallel to the glass capillary array: the linear transfer mechanism positions the gas deposition system 5 mm in front of the Ag wafer. One hour later, the experimental setup is baked 24 h, the emission of the QMS switches on and the IONIVAC is adjusted. The apparatus cools to room temperature within three hours and the compressor of the closed cycle helium refrigerator starts to transfer heat from both stages. Nevertheless, operating the cold head without heating the 10 K stage would result in condensing residual gases onto the baked Ag-(111) wafer. Hence, this stage must be held the first two hours at 313 K: potential residual gases condense on the 30–40 K radiation shield without contaminating the substrate. Ultimate pressures yield $(4.2 \pm 0.9) \times 10^{-10}$ mbar, averaged over 21 experiments. Figure 5 displays a typical residual gas spectra with $m/z=1$ (H^+), 2 (H_2^+), 12 (C^+), 14 (N^+ , N_2^+), 16 (O^+), 17 (OH^+), 18 (H_2O^+), 28 (N_2^+ , CO^+), 44 (CO_2^+), 61.67/62.33 ($^{185/187}\text{Re}^{3+}$), 92.5/93.5 ($^{185/187}\text{Re}^{2+}$), and 185/187 ($^{185/187}\text{Re}^+$) at 3.5×10^{-10} mbar. It is worth mentioning that the ion current of H_2O is in the order of the rhenium peak subliming from the filament of the QMS; additionally, the chamber is absolutely free of hydrocarbons.

After generating UHV conditions and 10 K, the mass spectrometer controlled gas condensation takes place at 10^{-6} mbar for 30 min [$^{13}\text{CH}_4$, CH_4 , CD_4 , and CH_4/O_2 mixtures ($1 \pm 0.5\%$ O_2)] and 2 min (C_2H_2 , C_2H_4). Figure 6 shows typi-

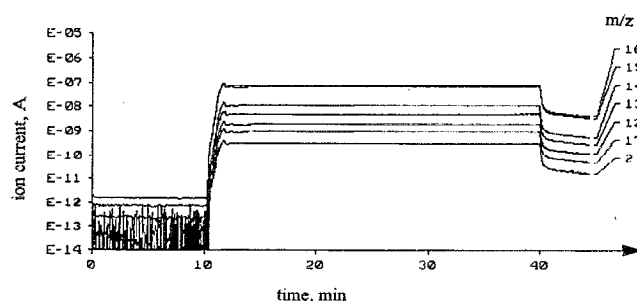


FIG. 6. Time-dependent ion currents of m/z 17 ($^{13}\text{CH}_4^+$), 16 ($^{13}\text{CH}_3^+/\text{CH}_4^+$), 15 ($^{13}\text{CH}_2^+/\text{CH}_3^+$), 14 ($^{13}\text{CH}/\text{CH}_2^+$), 13 ($^{13}\text{C}^+/\text{CH}^+$), 12 (C^+), and 2 (H_2^+) before, during, and after $^{13}\text{CH}_4$ condensation.

cal time-dependent ion currents underlining reproducible gas flows during all experiments. Nevertheless, the gas molecules hardly deposit in thermal equilibrium, hence, leading to regions of frozen high temperature modifications and amorphous solids. Well-defined modifications of the frosts are generated by keeping the cold finger at 10 K, then heating to 35 K with 0.005 K s^{-1} , equilibrating at 35 K for 1 h, and cooling down to 10 K with 0.005 K s^{-1} . In the case of CH_4 , phase II is produced with reproducible target thicknesses of $(4.8 \pm 0.9) \mu\text{m}$. The whole process is controlled via FTIR spectroscopy monitoring the rotational fine structure of ν_2 and ν_4 fundamentals of methane.^{31,32}

Further, the beam currents of the MeV protons and α particles are adjusted by the dummy unit. An aperture consisting of four magnetic deflectors and a wobbling system restricts the beam profile to a circular geometry of 2 cm diam, thus, covering an area of 3.14 cm^2 . During each irradiation the ion current is monitored on line by the nickel grid and, hence, guarantees a constant ion flux. The experimental error of $\approx 10\%$ is ruled by the grid's surface, i.e., 1.5% of the beam area; a closer nickel grid would reduce the experimental error, but influences the beam homogeneity dramatically. Experiments optimized the ion fluxes ϕ of 9 MeV α particles and 7.3 MeV protons to $\phi(\alpha) = 400 \text{ nA}\pi^{-1} \text{ cm}^{-2} = 127 \text{ nA cm}^{-2}$ and $\phi(p) = 350 \text{ nA}\pi^{-1} \text{ cm}^{-2} = 111 \text{ nA cm}^{-2}$, limiting the heating of the frost surfaces to $(4 \pm 1) \text{ K}$. All targets are irradiated isothermal at 10 K, i.e., simulating ices on interstellar grains or comets in Oort's cloud, or in the course of temperature program 10–50–10 K (beam on; 6 min at 10 K, heating to 50 K in 20 min with 2 K min^{-1} ; 34 min 50 K; beam off; cooling in 1 min with -40 K min^{-1} to 10 K), therefore simulating heated comets during their approach to sun or UV heated interstellar grains.

After the irradiation, the target is equilibrated 90 min at 10 K, heated to 70 K with $1/6 \text{ K min}^{-1}$, with 1 K min^{-1} to 298 K, and kept 60 min at 298 K. Higher heating rates should be avoided due to the thermal inertia of the system. Finally, the setup is vented with argon (99.9999%).

During the experiments and in the heating period, sublimating molecules are analyzed by a quadrupole mass spectrometer in the MID mode (monitored ion detection; recording of time profile of selected ion currents). The picked m/z values allow us to determine the molecules and residual gases quantitatively by matrix interval arithmetic. Here, only a brief summary is given. The detailed procedure is given in Ref. 33. A quadrupole mass spectrometer monitors ion currents, proportional to partial pressures in the case of nonoverlapping fragmentation pattern. Predominantly, however, fragments of different molecules add to a specific m/z -value, i.e., C_2H_4 , N_2 , and CO supply to $m/z=28$. i programmed m/z ratios are selected to result in an inhomogeneous system of linear equations including the measured ion current (right-hand vector), partial pressures of i gases (unknown quantity), and calibration factors of gases determined in separate experiments. Since all quantities are provided with experimental errors, matrix interval arithmetic, i.e., an IBM high accuracy arithmetic subroutine defining experimental uncertainties as intervals, is incorporated to extract quantitative infor-

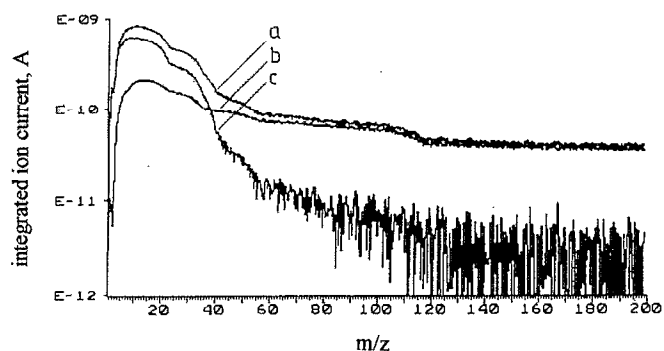


FIG. 7. Integrated mass spectra: (a) during heating phase, (b) background, (c) difference (a)–(b).

mation, thus, including experimental errors of m/z calibrations.

Additionally, complete spectra to $m/z=200$ are recorded in 10 min intervals. Interpretation of integrated mass spectra before the experiment (a), during the heating phase to 293 K after the irradiation (b), and the difference (b)–(a), (c), reveals $(0.8\% \pm 0.1\%)$ of synthesized molecules consist of masses greater than $m/z=200$, cf. Fig. 7. Consequently, the quadrupole mass analyzer is suitable for the experiments.

IR interferograms are accumulated over 6 min with 315 scans and 2 cm^{-1} resolution. All interferograms are transformed after the experiment achieving an increasing time resolution for kinetic studies. Care has to be taken to select background spectra for the ratioing procedure: in the first approximation, the Ag-(111) wafer constitutes a temperature dependent black body radiator. Therefore, a background spectrum of the wafer must be recorded in separate experiments every 10 K to get an optimal base line and eliminate temperature effects.

III. DISCUSSION

A. Experimental setup

Table I compiles the experimental conditions. The numbers in each row are averaged over all targets irradiated with identical ions, integrated ion fluences, and energies. The oxygen concentration is calibrated off line, i.e., depositing gas mixtures of 99.5% CH_4 and 0.5% O_2 five times, heating the frosts to 293 K, and analyzing data by matrix interval arithmetic. Finally, the dose D^* is defined in terms of absorbed energy in electron volts per molecule and computed according to Ref. 22.

Blank 1 analyzes potential contaminants, memory effects of earlier experiments, irradiation induced electronic interferences, and their influence on data recording. In the course of *blank 2*, CH_4 is deposited, cocondensates are determined, and the consequence of the rhenium ions impinging with kinetic energies of 0.2–0.3 eV on the frosts are analyzed. Nevertheless, neither contaminations nor memory effects influence the experimental results within the detection limits of the quadrupole analyzer and the FTIR. Moreover, synergistic effects of rhenium atoms and MeV ions are excluded by

TABLE I. Compilation of experimental parameters.

Target	Layer thickness, μm	Ion	Ion current, nA	Pressure, 10^{-10} mbar	Wafer temperature, K	Irradiation time, min	Integr. ion fluence, $\pi^{-1} \text{cm}^2$	Dose, eV
$^{13}\text{CH}_4$	4.0 ± 0.4	α	7.8 ± 0.5	4.8 ± 0.8	9.9 ± 0.2	60	$(4.4 \pm 0.3) \times 10^{15}$	29 ± 3
$^{13}\text{CH}_4$	4.2 ± 0.3	α	7.9 ± 0.6	4.1 ± 0.4	10.2 ± 0.4	300	$(2.2 \pm 0.2) \times 10^{16}$	145 ± 18
$^{13}\text{CH}_4$	4.1 ± 0.4	α	8.2 ± 0.8	5.2 ± 0.9	10.4 ± 0.4	60	$(4.6 \pm 0.4) \times 10^{15}$	30 ± 5
CD_4	5.5 ± 1.5	α	8.0 ± 0.2	4.8 ± 0.4	9.8 ± 0.1	60	$(4.5 \pm 0.2) \times 10^{15}$	30 ± 4
CD_4	6.0 ± 1.2	α	7.6 ± 0.5	5.2 ± 0.5	9.6 ± 0.1	300	$(2.1 \pm 0.1) \times 10^{16}$	144 ± 26
CD_4	6.5 ± 0.9	α	7.7 ± 0.3	2.8 ± 0.3	9.7 ± 0.1	60	$(4.3 \pm 0.2) \times 10^{15}$	29 ± 4
CH_4	4.3 ± 0.5	α	8.3 ± 0.2	3.3 ± 0.3	9.1 ± 0.1	60	$(4.7 \pm 0.1) \times 10^{15}$	29 ± 2
CH_4	4.0 ± 0.4	p	7.0 ± 0.5	3.7 ± 0.4	9.6 ± 0.1	336	$(4.0 \pm 0.3) \times 10^{16}$	28 ± 3
CH_4/O_2 (1%-2% O_2)	6.9 ± 0.7	α	7.8 ± 0.5	5.5 ± 1.0	11.0 ± 0.5	60	$(4.4 \pm 0.3) \times 10^{15}$	28 ± 5
CH_4/O_2 (1%-2% O_2)	4.8 ± 0.5	α	7.5 ± 0.5	4.3 ± 0.4	10.8 ± 0.1	300	$(2.3 \pm 0.3) \times 10^{16}$	136 ± 25
CH_4/O_2 (1%-2% O_2)	4.8 ± 0.6	α	7.6 ± 0.6	5.1 ± 1.2	10.8 ± 0.1	60	$(4.3 \pm 0.3) \times 10^{15}$	28 ± 5
CD_4/O_2 (1%-2% O_2)	6.4 ± 0.8	α	7.8 ± 0.3	4.1 ± 0.4	9.7 ± 0.1	60	$(4.4 \pm 0.2) \times 10^{15}$	30 ± 5
Blank 1	...	α	8.0 ± 0.5	3.5 ± 0.4	10.1 ± 0.1	90	$(6.7 \pm 0.4) \times 10^{15}$...
Blank 2	5.3 ± 0.4	2.4 ± 0.3	9.9 ± 0.1

performing irradiation with and without the emission of the rhenium filament.

A comparison with Table II, summarizing experimental conditions of other modern simulation chambers, reveals definitely the uniqueness of the designed experimental setup as well as combined reproducible experimental conditions, i.e., temperature ($\bar{\varnothing}=10$ K, $\sigma=0.5$ K), pressure ($\bar{\varnothing}=4.2 \times 10^{-10}$ mbar, $\sigma=0.9 \times 10^{-10}$ mbar), and the ion current ($\bar{\varnothing}=8$ nA, $\sigma=0.3$ nA). On the other hand, different machines operate at pressures $>10^{-9}$ mbar and, hence, cannot eliminate cocondensations of residual gases and hydrocarbon contaminations emerging from their roughing pumps. Further, no temperatures are monitored during irradiations; tem-

peratures in the course of experiments, included in parentheses, were estimated roughly, but a general trend of temperature rising as a result of excessive ion fluence and insufficient target cooling is evident.

B. Influence of target temperature on product distribution

All irradiation increased the temperature of the Ag-(111) crystal in (0.2 ± 0.1) K, i.e., less than the experimental errors of the silicon diode. Consequently, the temperature of the silver substrate was restricted to (10 ± 0.5) K, whereas the surface layer of the frosts were heated by ions to (14 ± 1) K,

TABLE II. Compilation of experimental parameters during ion irradiation of methane targets; ? : no information available.

No.	Target	Target thickness, μm	Ion	Energy, MeV	Flux, $\text{cm}^{-2} \text{s}^{-1}$	Ion current, $\mu\text{A cm}^{-2}$	Fluence, cm^{-2}	Dose, eV	Penetration, μm	Pressure, mbar	Temperature, K	References
1	$^{13}\text{CD}_4$	0.07-3	H^+	1.5	$6E13$	10	$3.5E16$	285	63.3	$1E-8$	12(28)	34-35
2	$^{13}\text{CD}_4$	0.07-3	He^+	1.5	$6E13$	10	$3.5E16$	285	9.5	$1E-8$	12(28)	34-35
3	CD_4	0.07	H^+	0.06	$(3-6)E14$	50-100	?	?	1.2	$1E-8$	15	34-35
4	CH_4	?	H^+	0.1	$(3-6)E14$	50-100	$1E15$?	1.7	$1E-7$	10	36-38
5	CH_4	?	H^+	1	$(3-6)E14$	50-100	$1E15$?	32.3	$1E-7$	10	36-38
6	CH_4	?	H^+	1.5	$(3-6)E14$	50-100	$1E15$?	63.3	$1E-7$	10	37-38
7	CH_4	0.1-2	He^+	1	$(3-6)E14$	50-100	$1E15$	85	6.4	$1E-7$	10	39
8	CH_4	?	H^+	1.5	$5E12$	0.8	$7E16$	500	63.6	$1E-8$	10(27)	40,41
9	CH_4	0.4-15	H^+	1.5	$3E12$	0.5	$5E16$	340	63.3	$1E-7$	10	42,43
10	CH_4	10	H^+	1.5	$3E12$	0.5	$1E17$	680	63.3	$1E-7$	10	44,45
11	CH_4	18	H^+	1.5	$3E12$	0.5	$1E17$	250	63.3	$1E-7$	10	44-46
12	CH_4	?	H^+	1	$5E12$	0.8	$4E16$?	32.3	$1E-7$	10	46
13	CH_4	?	He^+	0.2	$5E12$	0.8	$4E16$?	2	$1E-7$	10	46
14	CH_4	?	Ar^+	0.05-0.2	$5E12$	0.8	$4E16$?	0.12-0.44	$1E-7$	10	47
15	CH_4	?	H^+	0.06	$(3-6)E14$	50-100	?	?	1.2	$1E-7$	15	47
16	CH_4	?	H^+	0.06-0.08	$6E13$	10	?	?	1.2-1.7	$1E-7$	20	48
17	CH_4	?	He^+	0.06-0.08	$6E13$	10	?	?	0.9-1.1	$1E-7$	20	48
18	CH_4	?	Ar^+	0.06-0.08	$6E13$	10	?	?	0.14-0.18	$1E-7$	20	49,50
19	CH_4	1	H_2^+	0.04	?	?	$1E17$?	1	$1E-7$	35	51
20	CH_4	18	H^+	1.5	$(3-5)E12$	0.5-0.8	$2E16$	140	63.6	$1E-6$	15	44
21	CH_4	?	Ar^{13+}	60	$8E6$	$1.3E-6$?	?	32	$1E-9$	15	52
22	CH_4	11	H^+	17.6	$(1-2)E12$	0.25-0.5	$(0.2-5)E15$	<6.3	5230	$1E-7$	11(<50)	22,25,53,54
23	CH_4	11	$^3\text{He}^{2+}$	7.3	$(1-2)E15$	0.25-0.5	$(4-8)E11$	40-70	102	$1E-7$	11(<46)	22,25,54
24	CH_4	?	^{11}C	1.1	?	77	54
26	CH_4	1000	H^+	17.4	$3E12$	0.5	$1E13-1E16$	$1E-2-1E1$	5190	?	77	22

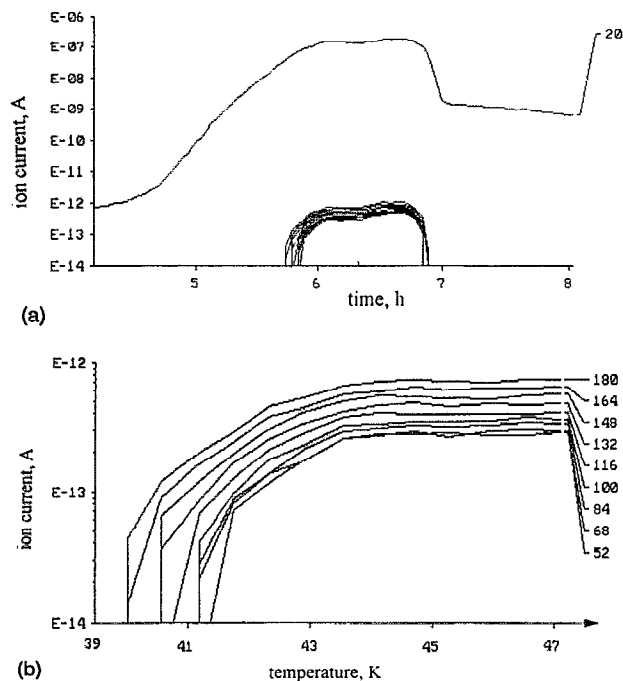


FIG. 8. Detected alkanes during matrix sublimation of CD_4 ($m/z=20$) after an irradiation at 10 K and $D^*=30$ eV. m/z 52, 68, 84, 100, 116, 132, 148, 164, and 180 (per-deutero-propane \rightarrow per-deutero-undecane) define molecular ions. (a) Survey, (b) magnification of $m/z > 20$.

giving an approximately linear temperature gradient $\Delta = (dT/dx)$, of $(-0.8 \pm 0.3) \text{ K } \mu\text{m}^{-1}$. Heating of irradiated targets after the experiment, however, does not go hand in hand with increasing molecular weights of subliming products (Fig. 8) as should be expected according sublimation increments of $+(15.6 \pm 2.7) \text{ K}$ per additional CD_2 unit in alkanes.²² Nevertheless, the sublimation sequence is reversed: $m/z=180$ ($\text{C}_{11}\text{D}_{24}$) is detected first, i.e., synthesized in target layers directly exposed to the ion beam [$T=(14 \pm 1) \text{ K}$], whereas per-deutero-propane is generated in volumes of $T=(10 \pm 1) \text{ K}$ attached to the Ag-(111) wafer. Quantitative analyses yield $\text{C}_{11}\text{D}_{24}$ to be formed 70%–100% in regions of $T=(13 \pm 2) \text{ K}$: the increasing molecular weight of alkanes coincides with production zones of higher

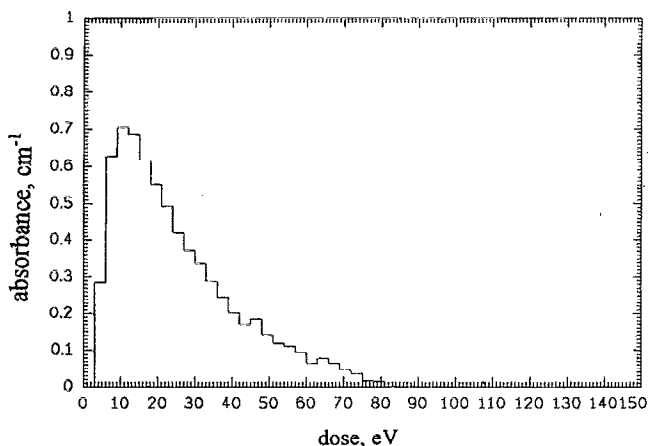


FIG. 9. Time-dependent integrated IR absorption of $\nu_2(\text{O}_2\text{H})$ during a 300 min α particle irradiation of a CH_4/O_2 target.

TABLE III. Detected molecules in residua of α particle irradiated CH_4/O_2 targets; 1: $T=10 \text{ K}$, $D^*=30 \text{ eV}$; 2: $T=50 \text{ K}$, $D^*=30 \text{ eV}$.

Molecule	Mass, pg		
	1	2	
1	R-O-TMS ^b	2.1/13.6	0.9/3.0
2	O[(CH_2) ₂₂ -O-TMS]	14.8/22.4	25.5/64.8
3	R-O-TMS	16.2/10.7	22.4/173.1
4	R-O-TMS	3.6/4.3	5.2/14.4
5	$\text{C}_{13}\text{H}_{27}$ -COO-TMS	2.7/3.0	7.9/18.6
6	R-COO-TMS	1.7/2.6	2.3/7.2
7	$\text{C}_{14}\text{H}_{29}$ -COO-TMS	8.5/36.1	11.7/109
8	R- C_6H_{13}	3.0/5.7	3.6/16.7
9	$\text{C}_{15}\text{H}_{31}$ -COO-TMS	11.3/10.1	52.7/83.9
10	$\text{C}_{17}\text{H}_{35}$ -COO-TMS	7.8/4.5	26.3/57.0
11	$\text{C}_{19}\text{H}_{39}$ -COO-TMS (primary acid)	0.3/2.6	7.1/15.9
12	$\text{C}_{19}\text{H}_{27}$ -COO-TMS (abietine acid)	1.5/6.5	15.0/30.1
13	R- C_4H_9 ^a	1.1/4.6	1.5/5.4
14	R- C_4H_9 ^a	1.3/3.4	1.5/4.5

^aNo OH groups; R: OCH-containing organic groups, identification impossible.

^bTMS=trimethyl silyl.

temperatures and underlines temperature-dependent reaction mechanisms, i.e., a diffusion controlled product distribution.

C. Contamination effects

Molecular oxygen serves as a radical scavenger, i.e., trapping of ion beam produced diffusive hydrogen and deuterium atoms, thus, reacting to O_2H followed by conversion to H_2O_2 , and H_2O . Equations (4) and (5) are derived from the time-dependent concentration profile $\nu_2(\text{O}_2\text{H})$, cf. Fig. 9:



Additionally, storage of reactive H atoms at 10–15 K leads to explosive pressure shocks from 10^{-10} to $\approx 10^{-3}$ mbar, ejecting up to 90% of the frosts into vacuum. Detailed computations define a critical concentration of mobile H atoms exceeding $(6\% \pm 3\%)$ as the limiting parameter determining these processes. On the other hand, trapping of diffusive hydrogen radicals in CH_4/O_2 targets eliminate these explosions, cf. Eqs. (4) and (5).

Further, only CH_4/O_2 frosts form brown to yellow residues comprising up to 5% of the deposited carbon, whereas pure methane targets never yielded any remnants after heating the irradiated frosts to 293 K. However, FTIR spectra of irradiated samples differ dramatically in the IR absorption region of $3800\text{--}2800 \text{ cm}^{-1}$, i.e., stretching vibrations of hydroxyl groups ($-\text{OH}$) in alcohols, carboxyl acids, and water in spite of identical experimental parameters. Analyses clearly indicate that the experimental error of preparing CH_4/O_2 mixtures affects the product distribution as corroborated by GC-MS detections of synthesized carboxyl acids

after dissolving the residues in dichloromethane and reaction to trimethyl silyl esters: absolute errors of 0.5% oxygen increases the yield of selected carboxyl acids up to 1000%, cf. Table III, thus underlining the need of UHV conditions to archive reproducible conclusions from the experimental results.

- ¹J. Geiss, *et al.*, in COSPAR Colloquia Series Vol. 3, edited by E. Marsch and R. Schwenn (Pergamon, New York, 1992).
- ²J. A. Simpson, in *Introduction to the Galactic Cosmic Radiation*, edited by R. Behrisch (Reidel, Amsterdam, 1983).
- ³R. E. Johnson, *Energetic Charged Particle Interactions with Atmospheres and Surfaces* (Springer, Berlin, 1990).
- ⁴W. L. Brown, L. J. Lanzerotti, and R. E. Johnson, *Science* **218**, 525 (1982).
- ⁵R. E. Johnson, L. J. Lanzerotti, and W. L. Brown, *Adv. Space Res.* **4**, 41 (1984).
- ⁶K. Roessler, in *Solid-State Astrophysics*, edited by E. Bussoletti and G. Strazzulla (North-Holland, Amsterdam, 1991).
- ⁷R. Smuluchowski, *Astrophys. Space Sci.* **75**, 1353 (1981).
- ⁸N. R. Lerner, E. Peterson, and S. Chang, *Geochim. Cosmochim. Acta* **57**, 4713 (1993).
- ⁹C. N. Matthews, presented on The World Space Congress, Washington, DC, 1992 (unpublished).
- ¹⁰R. Hayatsu and E. Anders, *Top. Cur. Chem.* **57**, 1 (1981).
- ¹¹M. Kaschke, M. J. Russell, and W. J. Cole, *Origins Life* **24**, 43 (1994).
- ¹²L. J. Lanzerotti, W. L. Brown, and K. J. Marcantonio, *Ap. J.* **313**, 910 (1987).
- ¹³G. Strazzulla, *Adv. Space Res.* **7**(5), 17 (1987).
- ¹⁴J. B nit, J. P. Bibring, S. Della-Negra, Y. Le Beyec, M. Mendenhall, F. Rocard, and K. Standing, *Nucl. Instrum. Methods B* **19/20**, 838 (1987).
- ¹⁵W. Schutte, Dissertation, University of Leiden, 1988.
- ¹⁶G. A. Baratta and G. Strazzulla, in *Dusty Objects in the Universe*, edited by E. Bussoletti and A. A. Vittone (Kluwer, Dordrecht, 1990).
- ¹⁷G. Strazzulla, G. A. Baratta, R. E. Johnson, and B. Donn, *Icarus* **91**, 101 (1991).
- ¹⁸M. H. Moore and R. Khanna, *J. Geophys. Res.* **96**, 17541 (1991).
- ¹⁹A. G. G. M. Tielens, L. J. Allamandola, and S. A. Sandford, in *Solid State Astrophysics*, edited by E. Bussoletti and G. Strazzulla (North-Holland, Amsterdam, 1991).
- ²⁰K. Roessler, *Nucl. Instrum. Methods B* **65**, 55 (1992).
- ²¹A. Hegazy, T. Sasuga, M. Nishii, and T. Seguchi, *Polymer* **33**, 2904 (1992).
- ²²R. I. Kaiser, Report No. J l-2856 (1993).
- ²³A. Patnaik, K. Roessler, and E. Zador, *Adv. Space Res.* **9**, 49 (1989).
- ²⁴K. Roessler, G. Eich, A. Patnaik, and E. Zador, *Lun. Plan. Sci. Conf. XXI*, 1035 (1990).
- ²⁵R. I. Kaiser, J. Lauterwein, P. M ller, and K. Roessler, *Nucl. Instrum. Methods B* **65**, 463 (1992).
- ²⁶G. Strazzulla, L. Calcagno, and G. Foti, *Il Nuova Cimento* **8**, 63 (1985).
- ²⁷J. M. Greenberg, University of Leiden, presented on COSPAR, Washington, DC, August 1992.
- ²⁸R. P. Reed and A. F. Clark, *Materials at Low Temperatures* (American Society for Metals, Metals Park, OH, 1983).
- ²⁹A. Kent, *Experimental Low-Temperature Physics* (MacMillan, London, 1993).
- ³⁰R. C. West, *Handbook of Chemistry and Physics* (Chemical Rubber Boca Raton, 1987).
- ³¹R. Wykhoff, *Crystal Structures* (Wiley, New York, 1965).
- ³²J. Pearl, M. Ngoh, M. Ospina, and R. Khanna, *J. Geophys. Res.* **96**, 17477 (1991).
- ³³R. I. Kaiser, P. Jansen, and K. Roessler, *Rev. Sci. Instrum.* (submitted).
- ³⁴R. E. Johnson, W. L. Brown, and L. J. Lanzerotti, *J. Chem. Phys.* **87**, 4218 (1983).
- ³⁵T. A. Tombrello, *Nucl. Instrum. Methods B* **24/25**, 517 (1987).
- ³⁶R. E. Johnson, L. J. Lanzerotti, W. L. Brown, W. M. Augustyniak, and C. Mussil, *Astron. Astrophys.* **123**, 343 (1983).
- ³⁷G. Strazzulla, L. Torrisi, and G. Foti, *Europhys. Lett.* **7**, 431 (1988).
- ³⁸T. Venkatesan, L. Calcagno, B. S. Elman, and G. Foti, in *Ion Beam Modification of Insulators*, edited by P. Mazzoldi and G. W. Arnold (Elsevier, Amsterdam, 1987), p. 301.
- ³⁹G. Strazzulla, *Icarus* **61**, 48 (1985).
- ⁴⁰G. Strazzulla, L. Calcagno, and G. Foti, *Astron. Astrophys.* **148**, 441 (1984).
- ⁴¹G. Strazzulla, R. S. Cataliotti, L. Calcagno, and G. Foti, *Astron. Astrophys.* **133**, 77 (1983).
- ⁴²L. J. Lanzerotti, W. L. Brown, C. G. MacLennan, A. F. Cheng, S. M. Krimigis, and R. E. Johnson, *J. Geophys. Res.* **92**, 949 (1987).
- ⁴³L. Calcagno, G. Foti, and G. Strazzulla, *Radiat. Eff.* **91**, 79 (1985).
- ⁴⁴L. Calcagno, G. Foti, L. Torrisi, and G. Strazzulla, *Icarus* **63**, 31 (1985).
- ⁴⁵L. Calcagno and G. Foti, *Nuovo Cimento* **12D**, 281 (1990).
- ⁴⁶L. Calcagno, D. J. Oostra, R. Pedrys, A. Haring, and A. E. de Vries, *Nucl. Instrum. Methods B* **17**, 22 (1986).
- ⁴⁷A. E. de Vries, R. Pedrys, R. A. Haring, A. Haring, and F. W. Saris, *Nature* **311**, 39 (1984).
- ⁴⁸R. Pedrys, D. J. Oostra, R. A. Haring, L. Calcagno, A. Haring, and A. E. de Vries, *Nucl. Instrum. Methods B* **17**, 15 (1986).
- ⁴⁹J. B nit, J.-P. Bibring, and F. Rocard, *Nucl. Instrum. Methods B* **32**, 349 (1988).
- ⁵⁰J. B nit, J.-P. Bibring, and F. Rocard, in *Materials Modification by High-Fluence Ion Beams*, edited by R. Kelly (Kluwer, Dordrecht, 1989), p. 123.
- ⁵¹T. M. Hall, A. Wagner, and L. F. Thompson, *J. Appl. Phys.* **53**, 3990 (1982).
- ⁵²M. Behar, L. Amaral, J. R. Kaschny, and F. C. Zawislak, *Phys. Lett. A* **148**, 104 (1990).
- ⁵³R. I. Kaiser and K. Roessler, *Annu. Geophys.* **10**, 222 (1992).
- ⁵⁴R. I. Kaiser, R. M. Mahfouz, and K. Roessler, *Nucl. Instrum. Methods B* **65**, 447 (1992).